Diffusion behavior of lanthanide-additive compounds (Ce$_4$Sb$_3$, Ce$_2$Sb, and CeTe) against HT9 and Fe

Yi Xie[a,b], Jinsuo Zhang[a,*], Michael T. Benson[b], Robert D. Mariani[b]

[a] *Nuclear Engineering Program, Mechanical Engineering Department, Virginia Tech, Blacksburg, VA 24060, USA*
[b] *Idaho National Laboratory, P.O. Box 1625, MS 6188, Idaho Falls, ID 83415, USA*

ABSTRACT

Antimony and tellurium have been identified as promising additives in metallic fuel, which can immobilize free-lanthanide fission products into stable intermetallic compounds in order to mitigate the fuel-cladding chemical interaction. Ce$_4$Sb$_3$, Ce$_2$Sb, and CeTe are the primary compounds formed by Sb or Te with the lanthanide Ce present in the fuel. If these compounds are present at the outer periphery of the fuel, they will come in contact with and react with the cladding after the fuel swells. The present study investigates the reactivity of these compounds with two cladding materials, HT9 and Fe. The diffusion couple tests between these compounds and HT9 or Fe were conducted at 853 K. Scanning electron microscopy and transmission electron microscopy were used to analyze the morphology, microstructure, and phase distribution of the diffusion region. It was observed that the diffusion region thickness formed by the three compounds was significantly reduced compared to free Ce. There was no observed diffusion or reaction between Ce$_4$Sb$_3$ or Ce$_2$Sb with either HT9 or Fe. CeTe was found to diffuse and react with HT9, forming Cr$_3$Te$_4$ and TeFe at the diffusion region, as well as to penetrate into Fe, mostly by intergranular diffusion.

1. Introduction

Fuel-cladding chemical interactions (FCCIs) in metallic fuel result in the development of interaction layers that contain fuel, cladding, and fission product constituents, which will contain relatively low-melting phases and weaken the cladding strength [1]. Lanthanide fission products have been found to be one of the primary causes of FCCIs [2]. Caused by the radial temperature gradient in the irradiated fuel, lanthanides migrate to the outer periphery of the fuel and react with cladding. Lanthanides are free in the metallic fuel because they do not form intermetallic phases with the fuel constituents (e.g., U and Zr) based on the phase diagrams [3,4]. Hence, to mitigate FCCIs, tying up the lanthanides in the fuel is necessary.

One of the promising methods to mitigate FCCIs is to cast fuel additives into the metallic fuel [5]. The fuel additives, such as Sb [6], Te [7], Pd [5], Sn [8], and the Sb/Sn mixture [9], used to cast with the U-Zr fuel can combine with the lanthanides and form variable stable compounds. For instance, in the U-Zr-Sb-Ce alloys, Sb has been found to combine with Ce into stable compounds Ce$_4$Sb$_3$ and Ce$_2$Sb. While Sb is a thermal neutron poison, its effect on a fast neutron reactor is trivial due to the extremely small fast neutron cross section [10]. In the U-Zr-Te-Ce alloys, Te has been observed to combine with Ce and form CeTe.

The fuel matrix, composed of U and Zr, was not affected by the addition of Sb or Te.

The stable compounds consisting of fuel additives and lanthanides may be formed at the outer periphery of fuel, and will come in contact with the cladding after the fuel swells. Chemical interactions between the pure additive elements and the cladding material or constitute (e.g., HT9 and Fe) have been widely investigated. The diffusion of Sb into Fe has been reported [11]. Available studies concerning Te are more abundant than Sb. Both Te vapor and liquid have been recognized to corrode Fe-based alloys with forming two corrosion layers: the outer layer contained Fe tellurides and the inner layer contained Cr tellurides [12,13]. The substrate alloy was found to be penetrated/diffused intergranularly by Te, associated with a Cr depletion region at the corroding front [13]. Considering the active chemical interactions between Te and the cladding material, CeTe can potentially initiate chemical interactions with cladding, which is also a potential for Ce$_4$Sb$_3$ and Ce$_2$Sb. However, investigations on the chemical interaction between the compounds and HT9 and Fe are still lacking.

This study aims to analyze the potential chemical interactions between Ce$_2$Sb, Ce$_4$Sb$_3$, and CeTe (i.e., the Ce-phases found in the U-Zr alloy with Sb/Te addition [6,7]), and HT9 and Fe. Diffusion couple tests and microstructure analyses were carried out. A typical sodium-cooled

* Corresponding author at: 635 Prices Fork Rd, Blacksburg, VA 24060, USA.
E-mail address: zjinsuo5@vt.edu (J. Zhang).

fast reactor fuel/cladding interface temperature of 853 K was used in the diffusion couple test. Two types of diffusion couple tests were conducted: (I) diffusion couple tests between HT9 or Fe and Ce_2Sb, Ce_4Sb_3, or CeTe; and (II) direct diffusion couple test between HT9 and Ce. The Type-I test is representative of the compounds coming into contact with HT9/Fe. The Type-II test was performed to compare the diffusion behavior of components. The microstructure was analyzed focusing on the structure, morphology and phase distribution at the diffusion interface using a scanning electron microscope (SEM) and transmission electron microscope (TEM).

2. Experiment

2.1. Test samples

The samples used for the diffusion couple tests are Ce, Fe, HT9, Ce_4Sb_3, Ce_2Sb, and CeTe. The Ce, Fe, and HT9 samples were as-received. The Ce_4Sb_3, Ce_2Sb, and CeTe samples were fabricated in a laboratory. The sample preparation process is addressed in the following sections.

2.1.1. Ce, Fe, and HT9 samples

The Ce and Fe sheets were obtained from ESPI Metals, with a purity of 99.9 wt%. The grain size of Fe was about 50 μm. The Ce sheets were shipped from ESPI Metals within an Ar-filled can, and the Fe sheets were shipped in a common shipping package. Upon arrival at the laboratory, the sheets were stored in an Ar-filled glovebox (Model Inert PureLab 4 GB 2500 mm), where the oxygen level was less than 0.1 ppm, and the moisture level was less than 2 ppm, measured with the oxygen and moisture sensors of the glovebox system.

The HT9 sheet was obtained from Los Alamos National Laboratory. The alloy fabrication process is summarized: after casting the alloy under vacuum, the alloy plate was forged and rolled, and then hot rolled at 1173 K to a final thickness of 12.5 mm. Details about the fabrication process have been reported in literature [14]. The elemental composition is shown in Table 1. A TEM bright field (BF) image of the microstructure is shown in Fig. 1, which indicates the grain size to be roughly 1 μm.

The Ce, Fe, and HT9 samples used for the diffusion couple test were in the dimensions of $5 \times 5 \times 1$ mm, sliced from the as-received Ce, Fe, and HT9 sheets with an IsoMet™ low-speed precision cutter. The slicing was performed in an Ar-filled glovebox to protect the samples from oxidation.

The contact surface for the diffusion couple test was 5×5 mm, polished to 1 μm in the ambient environment. The samples were transferred to the glovebox immediately after polishing, and then rubbed on a napped polishing pad in the glovebox to remove any surface oxide prior to the test.
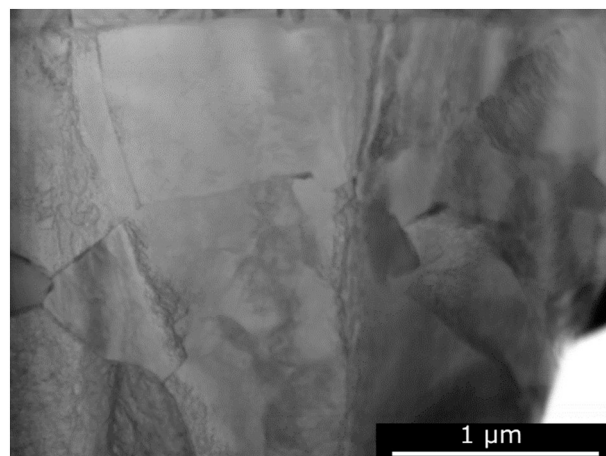
2.1.2. Ce_4Sb_3, Ce_2Sb, and CeTe samples

Ce rod and Sb shot were used to fabricate the Ce_4Sb_3 and Ce_2Sb samples. To fabricate CeTe, powder feedstock was used for both Ce and Te. Ce, Sb, and Te were all above 99.9 wt% pure, obtained from Alfa Aesar. Upon arrival, the materials were stored in the glovebox to

Fig. 1. TEM BF image of the HT9 sample indicating the grain microstructure. The grain size is about a micron.

protect them from oxidation. The samples were fabricated and prepared in an Ar glovebox to prevent oxidation.

The Ce_4Sb_3 and Ce_2Sb samples were fabricated using an arc melter. The Ce rod and Sb shot were mixed in the atomic ratio of 4-to-3 and 2-to-1, respectively for Ce_4Sb_3 and Ce_2Sb, and alloyed together in an arc melter. The resulting buttons were flipped and re-melted three times to ensure homogeneity. A portion of the buttons were mounted and polished for microstructural analysis with a SEM. Some of the buttons were ground into powder with an agate grinder and dispersed uniformly on an x-ray diffraction (XRD) holder plate for XRD analysis. The remaining samples were ground into powder and used for diffusion couple tests.

The CeTe sample was fabricated with a furnace, which can control the temperature and prevent Te loss. Using the arc-melting technique would result in a loss of Te, because the boiling temperature of Te is 1261 K. The melting temperature of Ce is 1068 K, thus melting Ce will cause Te to boil, which has been observed in previous work [7]. The fabrication process for the CeTe sample was to mix the Ce and Te powder in the atomic ratio of 1-to-1, heat at 1093 K for 0.5 h, and then at 853 K for 192 h. After the heat treatment, the sample was cooled in flowing Ar gas. The sample was in the form of porous bulk and granules after fabrication. Some of the sample was ground into powder to examine the composition and phase with a SEM and XRD, and the remaining sample was used for diffusion couple tests.

2.2. Diffusion couple tests

Four diffusion couple tests were conducted in the glovebox. Table 2 is a summary of the test material, procedure, and methods used to analyze the post-test samples.

Test 1 is a diffusion couple test between HT9 and Ce. The polished surfaces were facing each other and contacted. A significant diffusion region has been observed in the diffusion couple between Fe and Ce at 853 K for 72 h [15]. To have a direct comparison of the results for the HT9/Ce and Fe/Ce diffusion couples, the test time for the HT9/Ce diffusion couple was constrained to 72 h.

Table 1
Composition of the HT9 sample (hot-rolled).

Element	wt%	Element	wt%	Element	wt%
O	0.016	P	0.007	Si	0.39–0.40
N	0.031	Co	0.009	Cr	12.1
C	0.171	Cu	0.018	Mo	0.92
S	0.004	Ti	0.002	Ni	0.60
V	0.31	Fe	84.2	Al	0.006
W	0.58	Mn	0.59	–	–

Table 2
Summary of the diffusion couple tests conducted.

Test ID	Material	Temperature (K)	Time (h)	Post-test analysis
1	HT9/Ce	853	72	SEM
2	HT9/Ce_4Sb_3/Fe	853	192	SEM
3	HT9/Ce_2Sb/Fe	853	192	SEM
4	HT9/CeTe/Fe	853	192	SEM and TEM

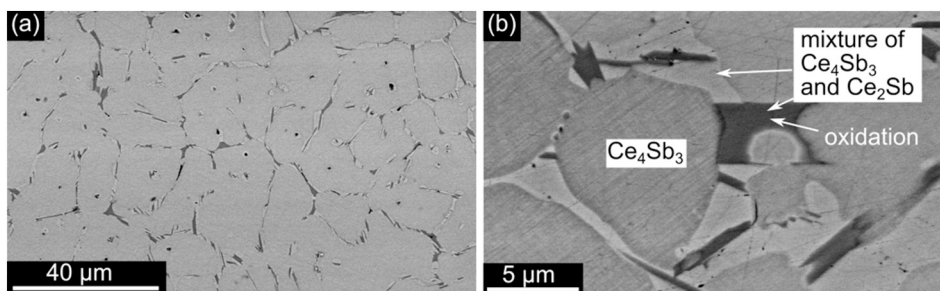**Fig. 2.** (a) Low-magnification SEM backscatter electron (BSE) image of the Ce$_4$Sb$_3$ sample, (b) high-magnification image indicating that the bulk phase is Ce$_4$Sb$_3$, and the intergranular region is the mixture of Ce$_4$Sb$_3$ and Ce$_2$Sb.

In Tests 2–4, the compound powder (Ce$_4$Sb$_3$, Ce$_2$Sb, or CeTe) was sandwiched between the HT9 and Fe samples to form a diffusion couple. These tests were run for 192 h, since the diffusion kinetics of compounds might be lower than pure Ce. Hence, the test time was expanded to 192 h to observe a more significant diffusion region.

Each diffusion couple sample was wrapped with Ta foil and clamped within a Kovar alloy jig. After the heat treatment, the diffusion couple samples were quenched in quenching oil to preserve the phases formed at 853 K. The surface of the Ce sample was visibly darkened after the test due to oxidation. It is noteworthy that an extremely small amount of oxygen would oxidize Ce even within an Ar-filled glovebox. In order to reduce the effect of oxidation, the diffusion couple center, which was tightly clamped and less affected by oxygen, was revealed for the microstructure analysis. Part of the diffusion couple was cut off, and rinsed in ethanol using an ultrasonic cleaner for 3 min to remove the compound powder that did not diffuse or react with HT9 and Fe. The sample was mounted with epoxy resin, and polished with SiC sandpapers and diamond solutions to 1 μm. After analyzing the as-polished surface with a SEM, the surface was etched with 2% nital etch for 30 s, followed by picral etch for another 30 s, and then analyzed again with a SEM. The HT9/CeTe/Fe sample (Test 4) was further analyzed using a TEM. The methods of using a SEM and TEM are discussed in Section 2.3.

2.3. Microstructure analysis

The as-cast Ce$_4$Sb$_3$, Ce$_2$Sb, and CeTe samples (Section 2.1.2), and post-test samples (Section 2.2) were studied using an XRD, SEM, and TEM to determine the microstructure and phase distribution.

An x-ray diffractometer (Model PANalytical X'Pert Powder) with copper source was used to identify the phases in the Ce$_4$Sb$_3$, Ce$_2$Sb, and CeTe (powder). The powder was dispersed on double-sided tape and attached to the silicon zero diffraction plate, and inserted into the XRD sample holder. The X'Pert Data Collector software was used to collect the data. The scan rate was 0.06°/s, and the step size was 0.2°/step.

A SEM (Model FEI Quanta 600 FEG) was used to analyze the microstructure. The accelerating voltage was 20 kV. The Bruker energy dispersive spectrometer (EDS) was equipped with a silicon drift detector (SDD), and the spatial resolution was 1–1.5 μm. EDS spectra were collected over the energy range of 0–10 keV, and analyzed using the Esprit 1.9 software. The measurement uncertainty of the EDS is a few percent of the measured value. A number of points for each investigated phase were measured to support the consistency of the EDS measurement. For the SEM analysis, the samples were mounted with epoxy resin, and polished by grinding the surfaces flat with SiC grinding paper followed by polishing with polycrystalline diamond suspensions, starting with 9 μm, 3 μm, and finally 1 μm.

A focused ion beam (Model FEI Helios 600 NanoLab) was used to prepare TEM samples at selected locations. A TEM (Model JEOL JEM2100 S/TEM) was used to analyze the microstructure at high magnifications. The operating voltage was 200 kV with point resolution at 0.23 nm and lattice resolution at 0.14 nm. TEM BF images were

captured with a GATAN UltraScan 1000XP camera. Selected area electron diffraction (SAED) patterns were captured with a GATAN Orius SC200D camera. Elemental mappings were obtained with a JEOL SDD-EDS. EDS spectra were analyzed using the Analysis Station program.

3. Results

3.1. Sample condition before the test

The as-cast Ce$_4$Sb$_3$, Ce$_2$Sb, and CeTe were analyzed with a SEM and XRD to examine the phases present for the test. Since the compounds are all line compounds, the secondary phase present needs to be known prior to the diffusion couple test. Knowing the other phase present will allow the post-test results to be interpreted correctly. For example, a small phase fraction of Ce was found in the Ce$_2$Sb sample (see Section 3.1.2). The reactivity of Ce versus Ce$_2$Sb is substantially different, thus knowing there is Ce present is important in the post-test analysis.

3.1.1. Ce$_4$Sb$_3$

The microstructure of the Ce$_4$Sb$_3$ sample is shown in Fig. 2. The bulk matrix consists of 57 Ce and 43 Sb (at.%) based on the EDS result, and thus is identified as Ce$_4$Sb$_3$. The darker, intergranular region is a small volume fraction of the sample, with the Ce and Sb in the ratio of 1.8 to 1. Based on this ratio, the phase is a mixture of Ce$_2$Sb and Ce$_4$Sb$_3$. Some areas of the intergranular region are darker due to oxidation. A small amount of oxidation may be present due to the Ce rod used during fabrication, which had some surface oxidation, or this could be surface oxidation occurring preferentially on Ce$_2$Sb, which has a higher atom fraction of Ce. The oxides could not be identified by XRD, though, so are present in very small amounts and should not affect the diffusion couple test.

The XRD pattern of the sample is shown in Fig. 3. The highest density peaks match well with the Ce$_4$Sb$_3$ reference pattern, indicating that Ce$_4$Sb$_3$ is the major phase of the sample. The Ce$_2$Sb density peaks were also found, though small. A few of the small density peaks at the
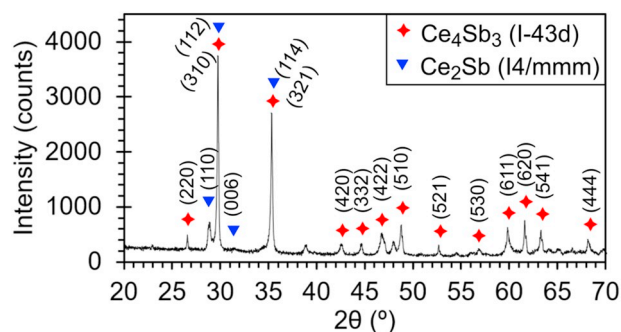

Fig. 3. XRD pattern of the Ce$_4$Sb$_3$ alloy. The sample is mostly composed of Ce$_4$Sb$_3$ with a small amount of Ce$_2$Sb. Oxides could not be identified. Crystal structures were obtained from Refs. [17, 18].

Table 3
Crystal parameters for phases identified in the Ce-Sb/Te alloys.

Phase	Space group	Cell parameters	Reference
Ce_4Sb_3	*I-43d* (220)	a = b = c = 0.956 nm	[17]
		α = β = γ = 90°	
Ce_2Sb	*I4/mmm* (139)	a = 0.455 nm	[18]
		c = 1.784	
		α = β = γ = 90°	
Ce	*Fm-3m* (225)	a = b = c = 0.516 nm	[19]
		α = β = γ = 90°	
CeO_2	*Fm-3m* (225)	a = b = c = 0.541 nm	[20]
		α = β = γ = 90°	
CeTe	*Fm-3m* (225)	a = b = c = 0.636 nm	[21]
		α = β = γ = 90°	
Ce_3Te_4	*I-43d* (220)	a = b = c = 0.953 nm	[22]
		α = β = γ = 90°	

Fig. 5. XRD pattern of the Ce_2Sb sample. The sample is mostly composed of Ce_2Sb, and a small amount of Ce and CeO_2. Crystal structures were obtained from Refs. [18–20].

large angle (64–70°) are close to the background level, and thus are not identified. XRD reference peaks were calculated with ReciprOgragh [16] using known crystal parameters listed in Table 3 and a copper source at 1.541 Å.

3.1.2. Ce_2Sb

The microstructure of the Ce_2Sb sample is shown in Fig. 4. The bulk matrix consists of Ce and Sb in a 2:1 ratio based on the EDS result, identified as Ce_2Sb. The backscatter image of the bulk matrix shows lighter and darker areas. The darker regions are oxidized to some extent. It is noteworthy that the Ce_2Sb sample is rich with Ce, so oxidation is inevitable. Oxides may be from the oxides on Ce feedstock, or caused by the uneven surface oxidation when transferring and analyzing with a SEM, or both.

The XRD pattern of the sample is shown in Fig. 5. The intensity peaks support the assessment that this sample is mainly composed of Ce_2Sb, with a smaller amount of Ce and CeO_2. Based on the SEM and XRD results, the alloy composition is between metallic Ce and Ce_2Sb in the Ce-Sb binary phase diagram [23].
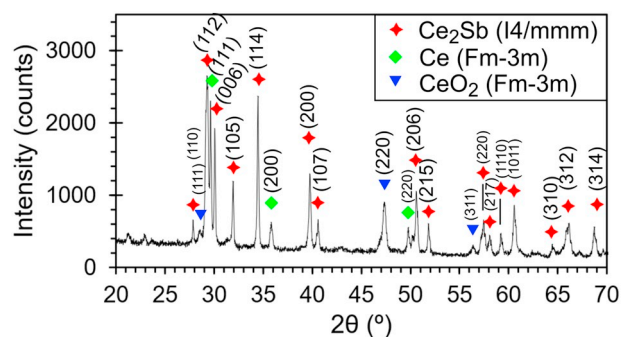
3.1.3. CeTe

The as-cast CeTe sample was composed of porous bulk and granules, shown in Fig. 6. The average composition of the sample is 48 Ce and 52 Te (at.%) based on the EDS analysis. The XRD pattern of the CeTe sample is shown in Fig. 7. The highest intensity peaks match well with the reference peaks of CeTe [21], while the other intensity peaks match well with the reference peaks of Ce_3Te_4 [22]. Therefore, the major phase is CeTe, with Ce_3Te_4 as a minor component, placing the composition at slightly Te-rich in the Ce-Te binary phase diagram [24].
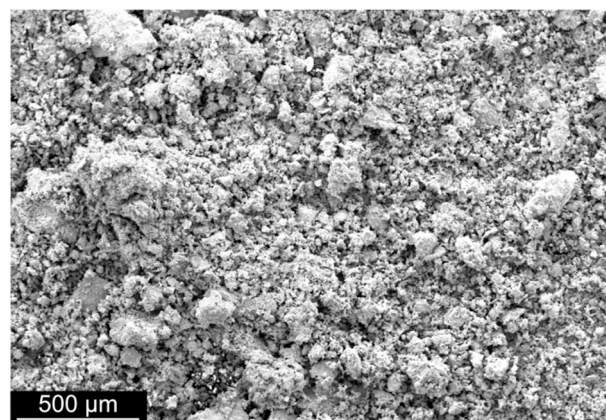
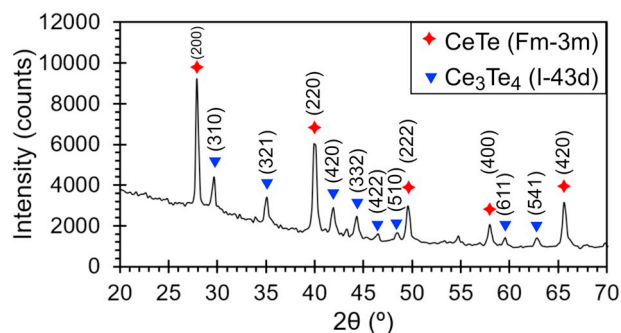### 3.2. Post-test results

3.2.1. HT9/Ce interface

The HT9/Ce interface is shown in Fig. 8(a), with Ce on the left and HT9 on the right of the image. The EDS line measurement across the
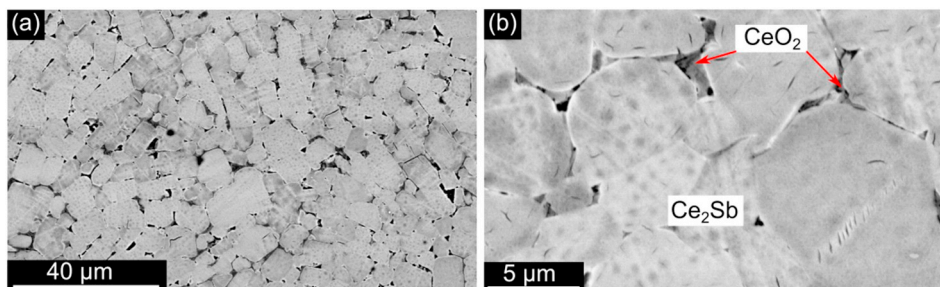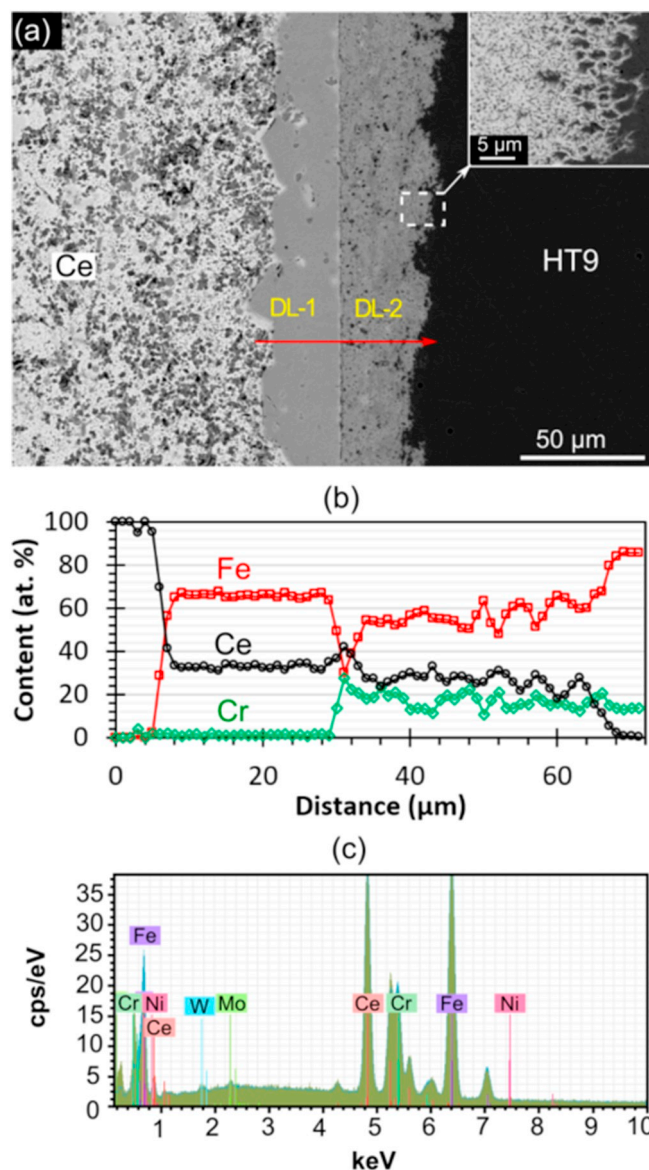

Fig. 6. SEM BSE image of the CeTe sample.

Fig. 7. XRD pattern of the CeTe sample. The sample is mostly composed of CeTe, with a small amount of Ce_3Te_4. Crystal structures were obtained from Refs. [21, 22].
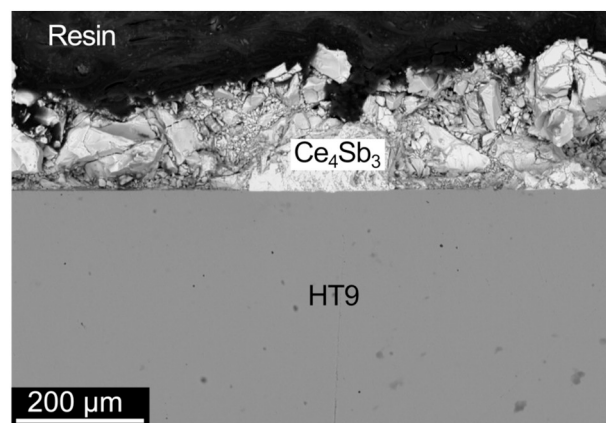

Fig. 4. (a) Low-magnification SEM BSE image of the Ce_2Sb sample, (b) high-magnification image indicating that the bulk matrix is Ce_2Sb, and the dark areas are CeO_2.

Fig. 9. SEM BSE image of the HT9/Ce$_4$Sb$_3$ interface. The interface boundary is flat and smooth. No evidence of any diffusion phases.

indicates the contact of two polished surfaces. The microstructures of DL-1 and DL-2 are various; the DL-1 phase is uniform, while the DL-2 phase is porous (see magnification in Fig. 8(a)). Due to the two characteristics, the boundary has to be the original interface.

Since DL-1 and DL-2 are located on each side of the original interface boundary, they are formed by the diffusion of Fe into Ce, and the diffusion of Ce into HT9, respectively. The formation of CeFe$_2$ in DL-1 results in the decrease of Fe in DL-2, which is consistent with the previous study where Fe in the cladding material rapidly migrated into Ce, leaving an Fe-depleted region into which Ce diffuses [25]. The Cr content in DL-2 is much higher than HT9 due to the reduction of Fe content.

3.2.2. HT9/Ce$_4$Sb$_3$ and Fe/Ce$_4$Sb$_3$ interfaces

The HT9/Ce$_4$Sb$_3$ interface is shown in Fig. 9. The two materials were contacted, but did not diffuse with each other. The post-test diffusion couple sample was cleaned using an ultrasonic cleaner. After cleaning, the Ce$_4$Sb$_3$ sample separated from the HT9 sample. The cross section of HT9 after the cleaning process is shown in Fig. 10. The roughness of the bounding surface, shown in Fig. 10, is about 1–3 μm, which was caused by the polishing damage before interaction. The bounding surface did not have any Ce or Sb diffusion based on the EDS analysis. An Fe- or Cr-depleted region was not observed, indicating Fe and Cr did not diffuse out of the HT9.

Fig. 8. (a) SEM BSE image of the HT9/Ce interface. From left to right, the left region is Ce, the two grey regions in the middle are diffusion layers (DL-1 and DL-2), and the black region is HT9. HT9 appears black in the image because the contrast between HT9 and Ce is too high. (b) EDS line scan data corresponding to the red arrow in (a). (c) Representative EDS spectra corresponding to the line scan data within distance 30–64 μm (i.e., DL-2 layer). (For interpretation of the references to colour in this figure legend, the reader is referred to the web version of this article.)

diffusion region is shown with a red arrow, with the corresponding EDS data shown in Fig. 8(b), and a representative EDS spectra shown in Fig. 8(c). The EDS spectra indicate the vast majority of elements are Ce, Fe, and Cr. Ni, W and Mo are minor elements of HT9, with extremely small energy peaks, corresponding to low single digit atomic percent in the alloy. Two diffusion layers (DL-1 and DL-2) were observed, one on each side of the interface. DL-1 consists of CeFe$_2$ with ~5 at.% Cr, based on the EDS analysis. DL-2 consists of Ce, Fe, and Cr, with Ce and Fe in the atomic ratio of 1-to-2, and the Cr content is about 25 at.%.

The boundary between DL-1 and DL-2 is the original interface boundary of HT9/Ce. Although an inert marker placed between two materials before interaction is commonly used to identify the original interface, the current study did not apply an inert marker because investigation of the original bounding surface is beyond the scope. Specifically, the boundary between DL-1 and DL-2 is flat, which
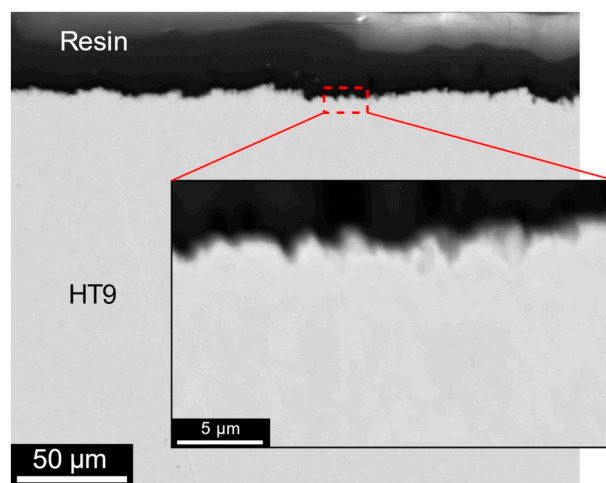

Fig. 10. SEM BSE image shows that Ce$_4$Sb$_3$ separated from HT9 after ultrasonic cleaning. The magnification indicates the surface roughness caused by the polishing damage before interaction.
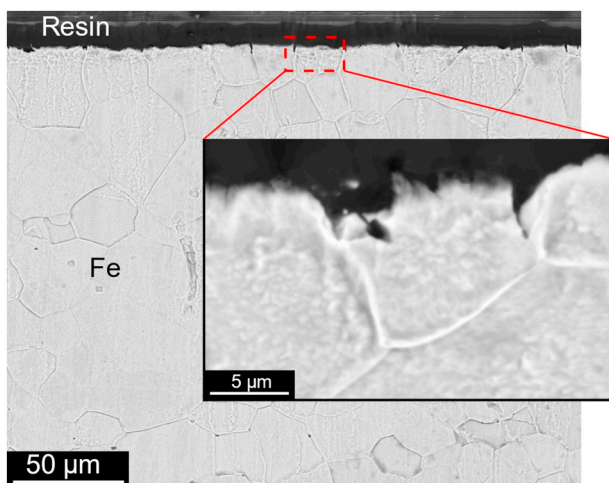
Fig. 11. SEM BSE image shows that Ce_4Sb_3 separated from Fe after ultrasonic cleaning. The magnification indicates the surface roughness caused by polishing damage before interaction. The observation surface was etched.
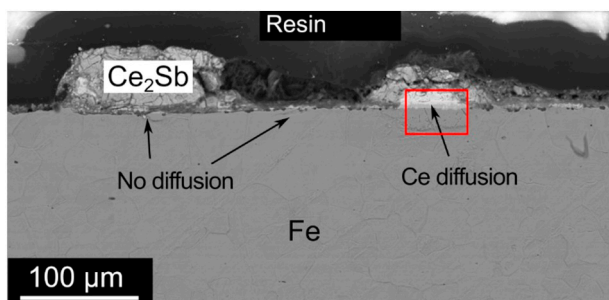

Fig. 12. SEM BSE image of the Fe/Ce_2Sb interface. Ce_2Sb was found to contact with Fe but not diffuse. The diffusion region caused by Ce is indicated, which corresponds to the high-magnification image shown in Fig. 13.
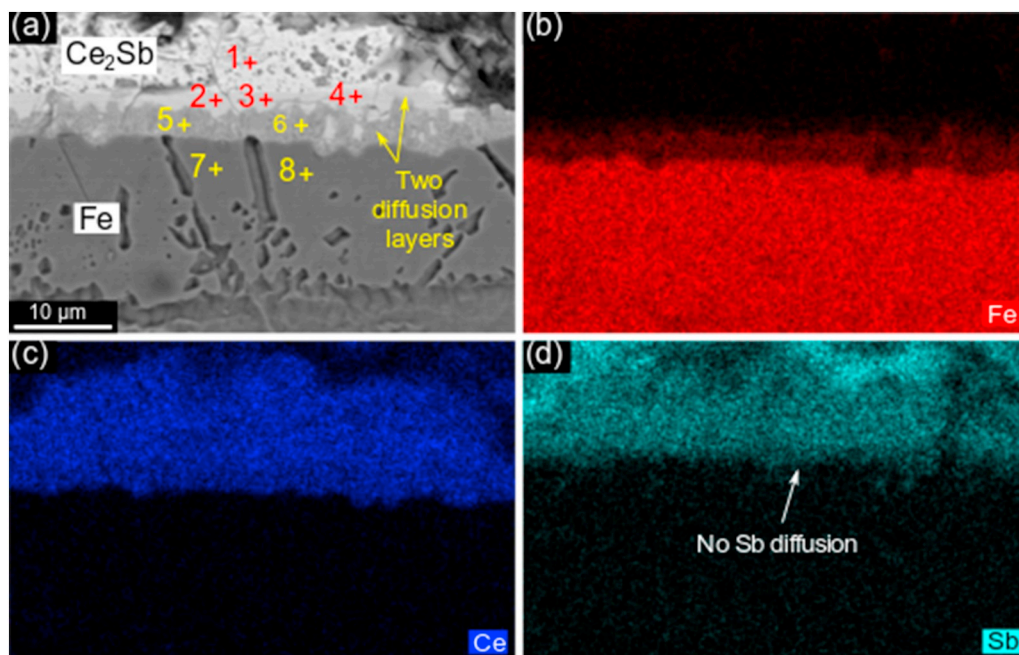
The Fe/Ce_4Sb_3 interface shows the same result. After cleaning, the Ce_4Sb_3 separated from Fe. The cross section of Fe is shown in Fig. 11. Only Fe was detected in the sample using the EDS analysis. There was no evidence of any adhering material or diffusion phases.

3.2.3. HT9/Ce_2Sb and Fe/Ce_2Sb interfaces

The Fe/Ce_2Sb interface is shown in Fig. 12. Most of the Fe/Ce_2Sb interface is free of diffusion. The small diffusion regions that are present were found to be a result of Ce diffusion, where Ce was a minor impurity in the Ce_2Sb sample.

The magnification of the Ce diffusion region (box in Fig. 12) is shown in Fig. 13, with the EDS data listed in Table 4. Two diffusion layers with a total thickness of about 10 μm were found. The diffusion layer next to the Ce_2Sb side (points 2–4) is composed of ~23 Fe, 17 Sb, and 60 Ce (at.%). Based on the EDS analysis and the ternary phase diagram of Ce-Fe-Sb [26], the diffusion layer is a mixture of Ce, $CeFe_2$, and Ce_2Sb. The other diffusion layer, next to the Fe side (points 5 and 6), is composed of ~72 Fe and 27 Ce (at.%), and identified as a mixture of $CeFe_2$ and Ce_2Fe_{17}, based on the EDS result and the binary phase diagram of Ce-Fe [23]. The Ce, present in $CeFe_2$ and Ce_2Fe_{17}, is the impurity phase in the Ce_2Sb sample. If the Ce is from the diffusion of Ce_2Sb, then a Ce-depleted area and a Sb-rich area, would have been found in the Ce_2Sb side; however, this is not the case.

Moreover, the composition measured by the EDS also supports the assessment that the diffusion region was formed by Fe-Ce interaction. In our previous study of the Fe/Ce diffusion couple [15], two diffusion layers were found. The diffusion layer on the Ce side had ~20 Fe and 80 Ce (at.%), and the other diffusion layer on the Fe side was composed of $CeFe_2$. The diffusion layers shown in Fig. 13 have the same microstructure and microchemistry as Fe/Ce diffusion. Therefore, the diffusion region was formed by Fe/Ce diffusion, caused by the Ce impurity in the Ce_2Sb sample. There was no evidence of any phases formed by Fe-Ce_2Sb interaction.

The same result was found in the HT9/Ce_2Sb interface. Diffusion was found at several locations along the interface. One instance is shown in Fig. 14. There are two diffusion layers, referred to as DL-1 and DL-2. The diffusion layer (DL-1) next to the Ce_2Sb side is composed of ~65 Fe and 35 Ce (at.%), while the other diffusion layer (DL-2) is next

Fig. 13. (a) Diffusion region corresponds to the box shown in Fig. 12 indicating two diffusion layers formed. (b–d) EDS mappings of Fe, Ce, and Sb. Diffusion of Sb to the Fe side was not observed, which indicates the diffusion layers were formed by Fe/Ce diffusion. The observation surface was etched. Corresponding EDS data are listed in Table 4.

Table 4
EDS data (at.%) for the points shown in Fig. 13.

|	Fe	Sb	Ce
1	0.3	34.5	65.1
2	22.1	15.6	62.4
3	23.1	17.5	59.4
4	23.2	19.5	57.3
5	73.0	0.2	26.9
6	70.1	0.1	29.8
7	99.8	0	0.2
8	99.8	0	0.2

to the HT9 side and composed of ~55 Fe, 25 Ce, and 20 Cr (at.%). The composition of the two layers is the same as the HT9/Ce diffusion layers (see Section 3.2.1). Sb was not in the diffusion layers, and a Ce-depleted region in the Ce$_2$Sb side was not observed. Therefore, the diffusion

region was formed by HT9/Ce diffusion. The Ce$_2$Sb phase did not show any indicator of diffusing with HT9.

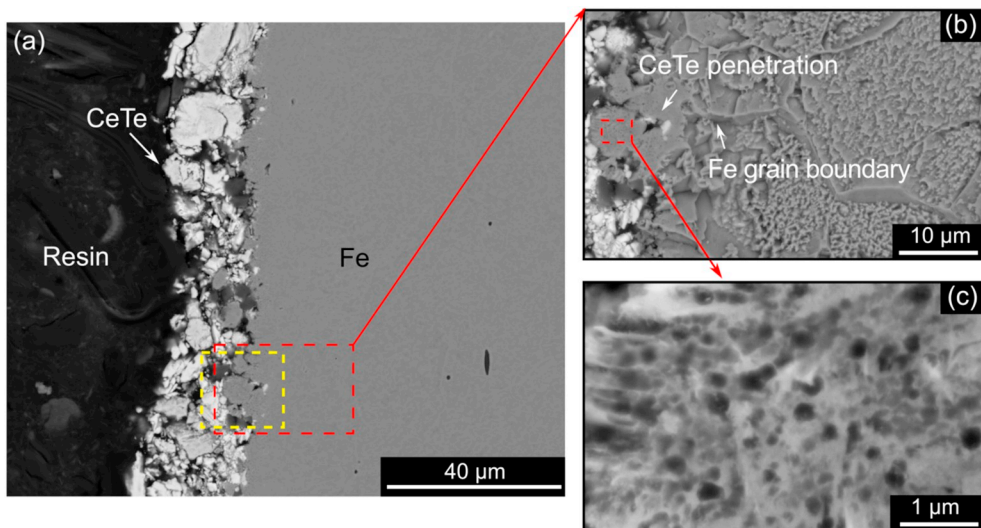### 3.2.4. Fe/CeTe interface

The Fe/CeTe interface is shown in Fig. 15, where the CeTe fully adhered to the Fe. The surface finish of the Fe sample was prepared to 1 μm, although after running the diffusion couple, the Fe contact surface became rough and porous as shown in Fig. 15(a). Note that under the SEM BSE mode, Fe is in grey contrast, and CeTe is bright white. Numerous white inclusions (i.e., CeTe) penetrated into the Fe.

The diffusion region is magnified, shown in Fig. 15(b), with the EDS mapping shown in Fig. 16. Based on the locations of Fe grains and grain boundaries, it was observed that CeTe penetrated into the Fe along the grain boundary. Two white inclusions, which are CeTe based on the EDS result, were trapped in the penetration path (adjacent to the end of path), shown in Fig. 15(b). The other portion of the penetration path is dark, which refers to voids/pores. These pores may be caused by the
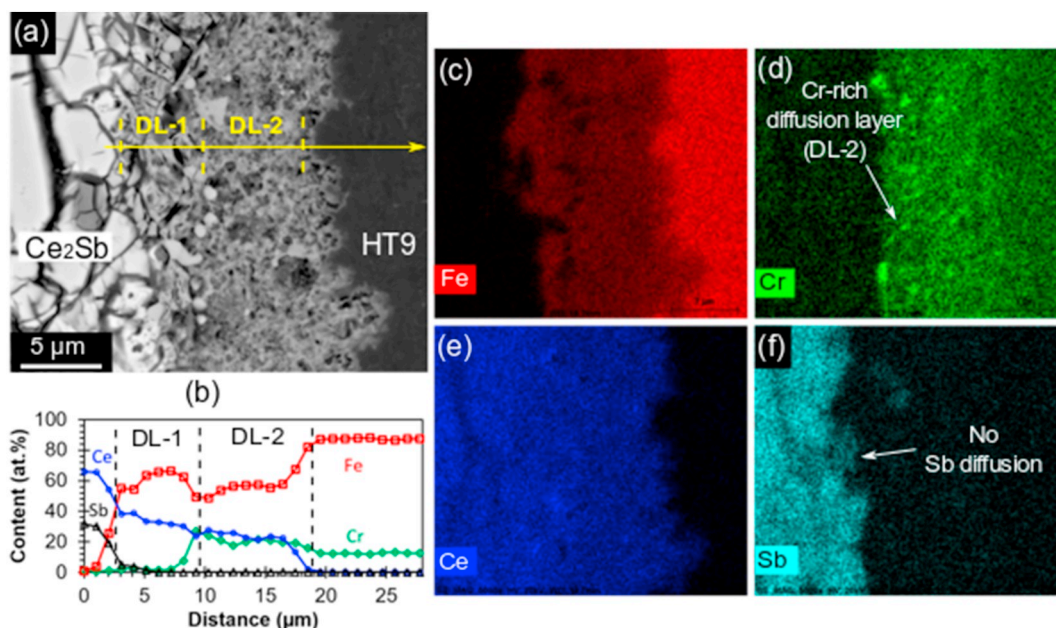

Fig. 14. (a) SEM BSE image of the HT9/Ce$_2$Sb interface with two diffusion layers (DL-1 and DL-2). (b) EDS line scan data correspond to the yellow arrow in (a); the composition indicates the diffusion layers were formed by HT9/Ce diffusion. (c–f) Elemental mappings of Fe, Cr, Ce, and Sb. Diffusion of Sb was not observed. (For interpretation of the references to colour in this figure legend, the reader is referred to the web version of this article.)

Fig. 15. (a) Fe/CeTe interface. (b) Magnification of the diffusion region corresponds to the red box in (a), showing the intergranular diffusion of CeTe. (c) Magnification corresponds to the red box in (b), showing numerous black inclusions (or pores) formed on the Fe grains adjacent to the interface boundary. (For interpretation of the references to colour in this figure legend, the reader is referred to the web version of this article.)
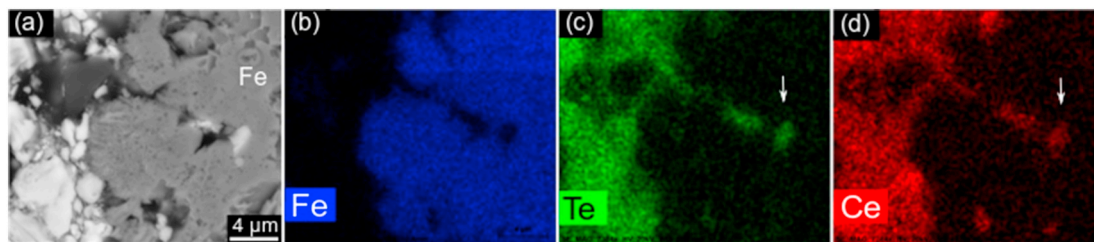
Fig. 16. (a) A closer look at the penetration (intergranular diffusion) of CeTe into Fe, corresponding to the yellow box in Fig. 15(a). (b–d) Elemental mappings of Fe, Te, and Ce, respectively. The arrows indicate the penetration of Te and Ce. (For interpretation of the references to colour in this figure legend, the reader is referred to the web version of this article.)
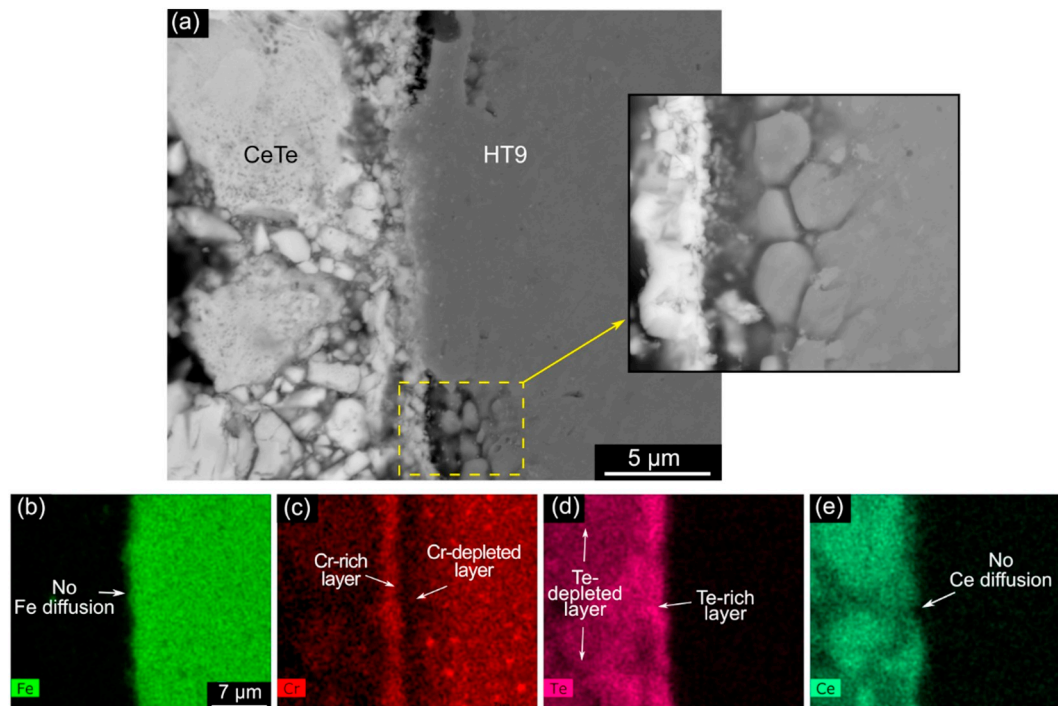
Fig. 17. (a) SEM BSE image of HT9/CeTe interface. (b–e) Elemental mappings of Fe, Cr, Te, and Ce corresponding to (a), respectively. The observation surface was etched.

SEM sample preparation that removed the inclusions from the pores.

Surrounding the penetration/diffusion path, the microstructure of Fe grains was changed, which is shown in Fig. 15(c). Numerous dark spots, roughly micron sized, were formed. They may be either diffusion/reaction products of Fe-CeTe interaction, or pores caused by Fe-CeTe reaction, which is unclear. The large-area EDS over the magnified region shown in Fig. 15(c), found about 3 at.% Ce and Te with the rest being Fe, supporting the assessment that CeTe diffused into the Fe grains.

3.2.5. HT9/CeTe interface

The HT9/CeTe interface is shown in Fig. 17. In the Cr EDS map, Fig. 17(c), there is a Cr-rich front moving into the CeTe, and a Cr-depleted region in HT9. In the Te EDS map, Fig. 17(d), there is a Te-rich area corresponding to the Cr-rich area on the CeTe side. Te appears to be depleted behind this Te-rich area. In the Ce EDS map, Fig. 17(e), there is a Ce-depleted area corresponding to the Cr-Te-rich area on the CeTe side. Ce appears to be moved backward by the diffusion of Cr. Diffusion of Fe was not observed. The TEM analysis on the Cr-Te diffusion layer was conducted as discussed below.

The TEM image of the Cr-Te diffusion layer is shown in Fig. 18, with the EDS data listed in Table 5, and corresponding SAED patterns shown in Fig. 19. In Fig. 18(a), material to the left is a Cr-depleted layer and to the middle/right is a Cr-Te diffusion layer. The Cr-depleted layer is mostly composed of Fe, and less than 5 at.% Cr (areas 1 and 2). The phase is identified as α-Fe based on the EDS and SAED results. The Cr-Te diffusion layer is mostly composed of ~55 Te and 39 Cr (at.%) (areas 3 and 4). The phase is identified as Cr_3Te_4 based on the EDS and SAED results. The small inclusions at the diffusion front of Te are the Te-Fe phase, which has about 41 Fe, 41 Te, and 15 Cr (at.%) (area 5). The phase is identified as TeFe based on the EDS and SAED results.

4. Discussion

The results of this study and previous work allowed us to compare the diffusion behavior of pure Ce and Ce-additive compounds on HT9 and Fe. Ce shows active chemical interaction with HT9 and Fe, while the Ce-bearing compounds significantly reduce the diffusion depth.

4.1. HT9/Ce and Fe/Ce

The HT9/Ce diffusion couple shows significantly different results with our previous study on Fe/Ce diffusion, which was run at the same test conditions (853 K for 72 h) [15]. The first obvious difference is the
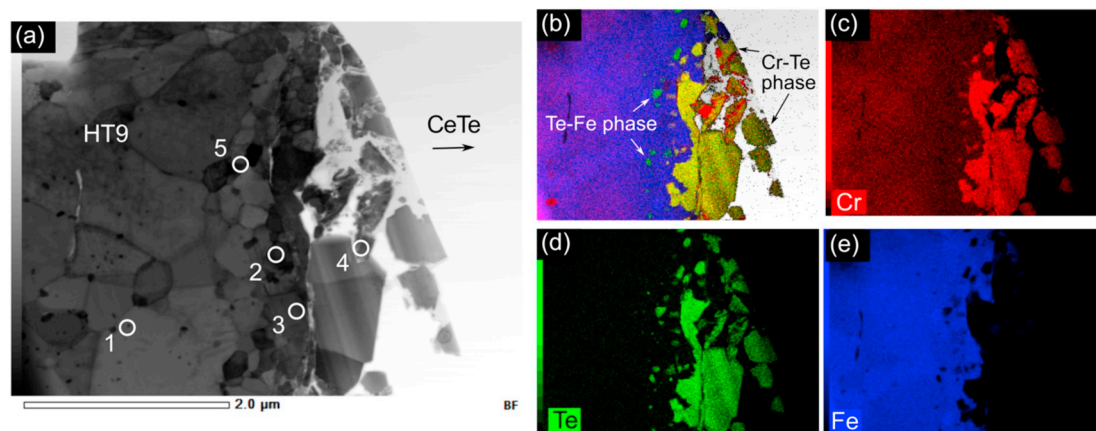
Fig. 18. (a) STEM BF image of HT9/CeTe interface. The left side shows that Cr in the HT9 grain matrix is depleted by diffusion, the middle/right side shows the diffusion layer. (b) Element overlay including Cr, Te, and Fe. (c–e) Elemental mappings of Cr, Te, and Fe, respectively. Corresponding EDS data are listed in Table 5.

Table 5
STEM-EDS data for the areas in Fig. 18(a) (at.%).

	Te	Ce	Fe	Cr	Ni	Mo	V	W	Phase
1	–	–	93.9	4.5	0.5	0.4	0.2	0.5	α-Fe[a]
2	1.8	–	93.1	2.1	2.5	0.6	–	–	α-Fe[a]
3	55.4	2.2	1.1	38.9	–	–	1.4	–	Cr_3Te_4[a]
4	57.2	1.0	1.1	39.5	–	–	–	–	Cr_3Te_4[b]
5	41.5	–	41.1	15.0	–	–	–	–	TeFe[a]

[a] Phase assignments based on diffraction analysis shown in Fig. 19.
[b] Suggested phase assignment based on STEM-EDS analysis.

Table 6
Space group and cell parameters of α-Fe, Cr_3Te_4, and TeFe phases used for indexing the diffraction patterns shown in Fig. 19.

Phase	Space group	Cell parameters	Reference
α-Fe	*Im*-3*m* (229)	a = b = c = 0.2865 nm	[27]
		α = β = γ = 90°	
Cr_3Te_4	*C*12/*m*1 (12)	a = 1.3916 nm	[28]
		b = 0.3932 nm	
		c = 0.6854 nm	
		α = γ = 90°	
		β = 118°	
TeFe	*P*4/*nmm* (129)	a = b = 0.3824 nm	[29]
		c = 0.6282 nm	
		α = β = γ = 90°	

diffusion direction in the diffusion couples. Fig. 8 shows interdiffusion between HT9 and Ce in both directions across the interface boundary. This was not the case for Fe/Ce, which only had diffusion from the Fe side into the Ce [15]. The discrepancy is possibly caused by the different grain sizes of HT9 and Fe. The grain sizes of HT9 and Fe samples are about 1 μm and greater than 20 μm, respectively, as shown in Figs. 1 and 15(b). Compared to Fe, HT9 provided a larger grain boundary area per unit volume for Ce diffusing along the grain boundaries, and thus resulted in the visible diffusion depths of Ce into HT9. The right top of Fig. 8(a) is the magnification of the diffusion front of Ce, showing the branching of the diffusion front of Ce, on the same scale as the HT9 grains, thus supporting the assessment that Ce diffused along the grain boundaries of HT9. It is noteworthy that the Cr in the HT9 sample does not preclude the diffusion of Ce, because Cr and Ce are immiscible and do not form intermetallic phases, based on the Cr-Ce binary phase diagram [30].

The second difference is the diffusion depth in the diffusion couples. In the present work, the total diffusion depth between HT9 and Ce is about 100 μm, split roughly even across the interface boundary. However, in the Fe/Ce diffusion couple, the diffusion depth in the Ce

side was much deeper, more than 540 μm [15]. The smaller diffusion depth in the Ce side in the present study is due to the Cr in HT9. A previous study on the interdiffusion between Ce and the 12Cr-Fe wt% alloy suggested that when Ce diffuses into the alloy, interacting with Fe, the Cr present would segregate and precipitate into a Cr-rich σ phase composed of Cr and Fe [31]. Because the σ-(Cr, Fe) phase consumes some of the available Fe at the interface, less Fe is available to diffuse into Ce, therefore slowing down the diffusion of Fe into Ce.

4.2. HT9/Ce-Sb and Fe/Ce-Sb

In the HT9/Ce-Sb or Fe/Ce-Sb diffusion couples, the Ce-Sb compounds do not exhibit diffusion with Fe or HT9. The result is consistent with our previous finding that Sb would prevent diffusion and subsequent reaction between Fe and Ce, due to the high thermodynamic stability of Ce-Sb intermetallics [15]. Sb has been found to diffuse with Fe [11]; however, the diffusion coefficient is much smaller than the lanthanides. Chemical interactions between Sb and Fe, including substrate penetration and intergranular diffusion, have not been reported. Sb is not likely an active diffusion agent to Fe or HT9.

Sb in the metallic fuel exhibits high thermodynamic stability with the fuel constituents, including lanthanides, and will not react with the cladding material. In the fresh fuel without burnup (i.e., U-Zr-Sb alloy), Sb has been found to combine with Zr into Sb-Zr intermetallics [6]. These Sb-Zr intermetallics are more stable than Fe-Sb,[1] so will not decompose to diffuse or react with Fe. In the irradiated fuel (i.e., U-Zr-Sb-Ce alloy), the Ce-Sb intermetallics are also more stable than Fe-Sb and Fe-Ce.[2] The present study indicates the Ce-Sb intermetallics do not decompose to diffuse or react with Fe and HT9 under the test condition.

4.3. HT9/CeTe and Fe/CeTe

CeTe is even more thermodynamically stable than the Ce-Sb compounds, with a more negative enthalpy of formation. However, CeTe behaves differently than the Ce-Sb compounds, which can be attributed to the strong chemical interaction between Te and Fe. The characteristics of CeTe reacting with Fe and HT9 are discussed in the following sections.

4.3.1. Fe/CeTe
CeTe penetration into Fe was observed in the study. The result is not

---

[1] Enthalpy of formation (kJ/g-atom): −117 for ZrSb [39], and −5 for $Fe_{1.27}Sb$ [40].
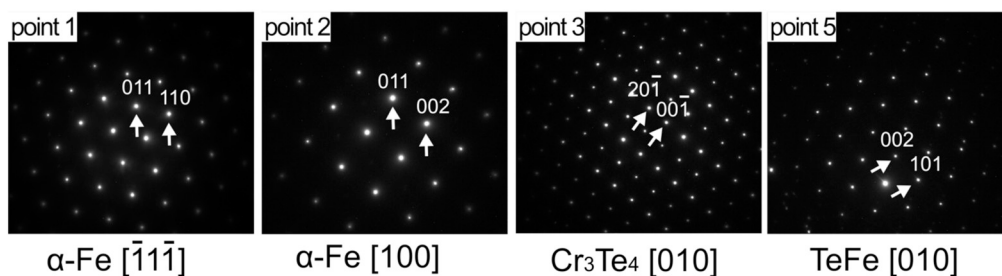[2] Enthalpies of formation (kJ/g-atom): −117 for Ce_4Sb_3 [18], and −27 for $CeFe_2$ [23].

Fig. 19. SAED patterns of α-Fe $[-11-1]/[100]$, Cr_3Te_4 [010], and TeFe [010] correspond to areas 1, 2, 3, and 5, respectively, shown in Fig. 18(a). The crystal parameters used for indexing the diffraction patterns are listed in Table 6.

surprising since pure Te has been found to preferentially diffuse along the grain boundaries [13,32], and form metal-tellurides at grain boundary regions [33,34]. However, pure Ce does not diffuse into Fe based on the result of Fe/Ce diffusion [15]. Hence, the penetration is a combined effect of both Ce and Te. The EDS maps, shown in Fig. 16, indicate Ce and Te remain together, with no Fe present, although the data are certainly not conclusive. The penetration depth for CeTe is much less than the penetration of pure Te at the same test condition, with the former being 10 μm or less, shown in Fig. 15, while the latter reached 100 μm or more [35]. The result indicates that the chemical interaction is caused by CeTe rather than pure Te.

However, it is unclear how CeTe would diffuse/react with Fe. The available thermodynamic data are insufficient to understand the reaction. Although the enthalpies of formation in the Ce-Te-Fe system are known, in the order $CeTe < CeFe_2 < TeFe$,[3] where $CeFe_2$ is the major reaction product of Fe/Ce diffusion, and TeFe is from the Fe/Te diffusion, the values of entropy of formation for some of the phases are lacking, so the free energy of reaction is unknown. Further investigation on the grains and grain boundaries, shown in Fig. 15, is needed to understand the mechanism.

4.3.2. HT9/CeTe

In the diffusion couple between CeTe and HT9, penetration of CeTe was not observed, instead, the data support a reaction between Cr and Te, indicating the CeTe compound is decomposing in the presence of Cr. Based on the microstructure and phase analysis, shown in Figs. 18 and 19, a pathway for the diffusion/reaction at the HT9/CeTe interface is proposed. The Cr present in HT9 at the interface diffuses into CeTe and reacts with CeTe to form Cr_3Te_4. Some of the surface CeTe may react with Fe and diffuse along the grain boundary, but that is a very small amount, probably decomposing when it comes in contact with Cr. In the Cr-Te diffusion/reaction region, the Ce present in CeTe is replaced by Cr, and moves toward the CeTe side since Ce does not form any intermetallic with Cr, based on the Cr-Ce phase diagram [30].

The preference of Cr-Te reaction over Fe-Te is because the Cr tellurides are more stable than the Fe tellurides (note the enthalpy of formation: Cr_3Te_4 is -34.5 kJ/g-atom [36], TeFe is -10 kJ/g-atom [37], both at 298 K). Accordingly, Cr diffuses to the outer periphery of HT9, and the Cr in the grain matrix is depleted by such diffusion.

HT9 is more resistant to the intergranular-type interaction compared to Fe, which ascribes to the Cr present in HT9. The Cr-Te diffusion layer retarded the outward diffusion of Fe, as shown in Fig. 18, which is consistent with the previous finding [38]. HT9 has fine grains, so the grain boundary per unit volume is also large. Due to this, the diffusion pathway of Cr from the HT9 matrix to the grain boundary is short, so Cr can be supplied easily with the reaction of ingressed Te at the grain boundary.

5. Conclusion

Sb and Te are both candidate fuel additives in metallic fuel, while the present study indicates that Sb would be a more robust option than Te because of the diffusion effect. Through investigating the diffusion of compounds (Ce_4Sb_3, Ce_2Sb, and CeTe) with HT9 and Fe, it was found that the diffusion/reaction depth is much less than Ce with HT9 or Fe. Specifically, the diffusion of Ce-Sb compounds with HT9 or Fe was not observed, which ascribes to the stable thermodynamic property of Ce-Sb compounds. CeTe, that has thermodynamic stability comparable to the Ce-Sb compounds; however, it was found to penetrate (mostly intergranularly diffuse) into Fe, and diffuse/react with HT9. The result is caused by the penetration/intergranular diffusion effect of CeTe on the Fe and HT9. The Cr present in HT9 can diffuse with CeTe, and replace the Ce to form Cr tellurides with Te. However, the mechanism of CeTe diffusing/reacting with Fe needs to be further investigated.

References

[1] G.L. Hofman, L.C. Walters, T.H. Bauer, Metallic fast reactor fuels, Prog. Nucl. Energy 31 (1997) 83–110, https://doi.org/10.1016/0149-1970(96)00005-4.

[2] Y. Xie, J. Zhang, X. Li, J.P. Isler, M.T. Benson, R.D. Mariani, C. Unal, Lanthanide migration and immobilization in metallic fuels, Prog. Nucl. Energy 109 (2018) 233–238, https://doi.org/10.1016/J.PNUCENE.2018.08.019.

[3] H. Okamoto, Ce-U (Cerium-Uranium), in: T.B. Massaiski (Ed.), Bin. Alloy Phase Diagrams, 2nd ed., ASM International, Materials Park, Ohio, 1990, pp. 1126–1127.

[4] N. Mattern, Y. Yokoyama, A. Mizuno, J.H. Han, O. Fabrichnaya, H. Wendrock, T. Harada, S. Kohara, J. Eckert, Experimental and thermodynamic assessment of the Ce–Zr system, Calphad 46 (2014) 213–219, https://doi.org/10.1016/J.CALPHAD.2014.05.002.

[5] R.D. Mariani, D.L. Porter, T.P. O'Holleran, S.L. Hayes, J.R. Kennedy, Lanthanides in metallic nuclear fuels: their behavior and methods for their control, J. Nucl. Mater. 419 (2011) 263–271, https://doi.org/10.1016/J.JNUCMAT.2011.08.036.

[6] Y. Xie, M.T. Benson, J.A. King, R.D. Mariani, J. Zhang, Characterization of U-Zr fuel with alloying additive Sb for immobilizing fission product lanthanides, J. Nucl. Mater. 498 (2018) 332–340, https://doi.org/10.1016/J.JNUCMAT.2017.10.039.

[7] Y. Xie, J. Zhang, M.T. Benson, J.A. King, R.D. Mariani, Assessment of Te as a U-Zr fuel additive to mitigate fuel-cladding chemical interactions, J. Nucl. Mater. 513 (2019) 175–184, https://doi.org/10.1016/J.JNUCMAT.2018.10.050.

[8] M.T. Benson, J.A. King, R.D. Mariani, M.C. Marshall, SEM characterization of two advanced fuel alloys: U-10Zr-4.3Sn and U-10Zr-4.3Sn-4Ln, J. Nucl. Mater. 494 (2017) 334–341, https://doi.org/10.1016/J.JNUCMAT.2017.07.057.

[9] M.T. Benson, Y. Xie, J.A. King, K.R. Tolman, R.D. Mariani, I. Charit, J. Zhang, M.P. Short, S. Choudhury, R. Khanal, N. Jerred, Characterization of U-10Zr-2Sn-2Sb and U-10Zr-2Sn-2Sb-4Ln to assess Sn + Sb as a mixed additive system to bind lanthanides, J. Nucl. Mater. 510 (2018) 210–218, https://doi.org/10.1016/J.JNUCMAT.2018.08.017.

[10] K. Shibata, Evaluation of neutron nuclear data on antimony isotopes, J. Nucl. Sci.

---

[3] Enthalpies of formation (kJ/g-atom): -155 for CeTe [41], and -10 for TeFe [37].

Technol. 51 (2014) 425–436, https://doi.org/10.1080/00223131.2013.872585.

[11] T. Sakuma, K. Yamazaki, T. Nishizawa, A characteristic dislocation network resulting from the diffusion of antimony into iron single crystals, Scr. Metall. 10 (1976) 687–691, https://doi.org/10.1016/0036-9748(76)90343-4.

[12] T. Arima, M. Takaki, I. Sato, K. Idemitsu, Y. Inagaki, H. Furuya, Reaction of modified SUS316 with tellurium under low oxygen potentials, Corros. Sci. 45 (2003) 1757–1766, https://doi.org/10.1016/S0010-938X(03)00022-2.

[13] R.J. Pulham, M.W. Richards, Chemical reactions of caesium, tellurium and oxygen with fast breeder reactor cladding alloys: Part I — the corrosion by tellurium, J. Nucl. Mater. 171 (1990) 319–326, https://doi.org/10.1016/0022-3115(90)90378-Z.

[14] P. Hosemann, S. Kabra, E. Stergar, M.J. Cappillo, S.A. Maloy, Micro-structural characterization of laboratory heats of the ferric/martensitic steels HT-9 and T91, J. Nucl. Mater. 403 (2010) 7–14, https://doi.org/10.1016/J.JNUCMAT.2010.05.005.

[15] Y. Xie, J. Zhang, M.T. Benson, R.D. Mariani, Thermodynamic stability studies of Ce-Sb compounds with Fe, J. Nucl. Mater. 499 (2018) 440–445, https://doi.org/10.1016/J.JNUCMAT.2017.12.008.

[16] N. Schoeni, G. Chapuis, ReciprOgraph, http://escher.epfl.ch.

[17] R. Nirmala, A.V. Morozkin, O. Isnard, A.K. Nigam, Understanding the magnetic ground state of rare-earth intermetallic compound Ce$_4$Sb$_3$: magnetization and neutron diffraction studies, J. Magn. Magn. Mater. 321 (2009) 188–191, https://doi.org/10.1016/J.JMMM.2008.08.102.

[18] A. Borsese, G. Borzone, D. Mazzone, R. Ferro, Heats of formation of Ce-Sb alloys, J. Less-Common Met. 79 (1981) 57–63, https://doi.org/10.1016/0022-5088(81)90051-5.

[19] J.D. Speight, I.R. Harris, G.V. Raynor, Alloys of cerium with neodymium, samarium and terbium, and of praseodymium with terbium, J. Less-Common Met. 15 (1968) 317–330, https://doi.org/10.1016/0022-5088(68)90191-4.

[20] N.K. Renuka, Structural characteristics of quantum-size ceria nano particles synthesized via simple ammonia precipitation, J. Alloys Compd. 513 (2012) 230–235, https://doi.org/10.1016/J.JALLCOM.2011.10.027.

[21] H.R. Ott, F. Hulliger, F. Stucki, Low-temperature thermal properties of rocksalt-type cerium compounds, Conf. Ser. Inst. Phys. 37 (1978) 72–78.

[22] A.V. Morozkin, R. Nirmala, O. Isnard, S.K. Malik, J. Yao, Y. Mozharivskyj, S.A. Granovsky, Magnetic ordering of anti-Th$_3$P$_4$-type R$_4$X$_3$ and Th$_3$P$_4$-type R$_3$X$_4$ compounds (R = Ce, Pr, Nd, Sm, X = Ge, Sb, Te), Intermetallics 19 (2011) 1794–1803, https://doi.org/10.1016/J.INTERMET.2011.07.019.

[23] X. Su, J.-C. Tedenac, Thermodynamic modeling of the ternary Ce–Fe–Sb system: assessment of the Ce–Sb and Ce–Fe systems, Calphad 30 (2006) 455–460, https://doi.org/10.1016/J.CALPHAD.2006.06.003.

[24] V.I. Chukalin, E.I. Yarembash, A.I. Villenskii, Phase diagram of the Ce-Te system, Inorg. Mater. 3 (1967) 1341–1347.

[25] J.H. Kim, J.S. Cheon, B.O. Lee, J.H. Kim, Interaction behavior between binary xCe-yNd alloy and HT9, J. Nucl. Mater. 479 (2016) 394–401, https://doi.org/10.1016/J.JNUCMAT.2016.07.040.

[26] D. Zhu, C. Xu, C. Li, C. Guo, R. Zheng, Z. Du, J. Li, Experimental study on phase relations in the Ce-Fe-Sb ternary system, J. Alloys Compd. 731 (2018) 1125–1139, https://doi.org/10.1016/J.JALLCOM.2017.09.276.

[27] S. Ohba, Y. Saito, Y. Noda, A measurement of charge asphericity in iron metal, Acta Crystallogr. Sect. A. 38 (1982) 725–729, https://doi.org/10.1107/S0567739482001454.

[28] S. Ohta, T. Kaneko, H. Yoshida, Anisotropic thermal expansion and effect of pressure on magnetic transition temperatures in chromium chalcogenides Cr$_3$X$_4$ with X = Se and Te, J. Magn. Magn. Mater. 163 (1996) 117–124, https://doi.org/10.1016/S0304-8853(96)00315-0.

[29] D. Fruchart, P. Convert, P. Wolfers, R. Madar, J.P. Senateur, R. Fruchart, Structure antiferroma gnetique de Fe$_{1.125}$Te accompagnee d'une deformation monoclinique, Mater. Res. Bull. 10 (1975) 169–174, https://doi.org/10.1016/0025-5408(75)90151-8.

[30] S.V. Terekhov, E.L. Korzun, Thermodynamic analysis of Ce-Cr melts, Russ. Metall. 4 (1988) 63–67.

[31] W.-Y. Lo, N. Silva, Y. Wu, R. Winmann-Smith, Y. Yang, Effects of Cr on the interdiffusion between Ce and Fe–Cr alloys, J. Nucl. Mater. 458 (2015) 264–271, https://doi.org/10.1016/J.JNUCMAT.2014.12.035.

[32] H. Cheng, Z. Li, B. Leng, W. Zhang, F. Han, Y. Jia, X. Zhou, Intergranular diffusion and embrittlement of a Ni–16Mo–7Cr alloy in Te vapor environment, J. Nucl. Mater. 467 (2015) 341–348, https://doi.org/10.1016/J.JNUCMAT.2015.09.053.

[33] H.E. McCoy, ORNL/TM-5920, Oak Ridge, TN (1978).

[34] J.R. Keiser, ORNL/TM-6002, Oak Ridge, TN (1977).

[35] T. Yutani, S. Nomura, S. Koyama, Y. Kuwajima, S. Ukai, High temperature chemical reactions of Fe-Cr-Ni and Fe-Cr cladding alloys by Te, I$_2$ and CsOH/CsI, J. Nucl. Mater. 201 (1993) 35–45, https://doi.org/10.1016/0022-3115(93)90157-T.

[36] F. Gronvold, E.F. Westrum, Thermodynamic aspects of the magnetic transitions in the chromium tellurides heat capacities of Cr$_5$Te$_6$, Cr$_3$Te$_4$ and Cr$_2$Te$_3$ from 5 to 350 K, Z. Anorg. Und Allg. Chemie. 328 (1964) 272–282, https://doi.org/10.1002/zaac.19643280510.

[37] C.-M. Arvhult, C. Guéneau, S. Gossé, M. Selleby, Thermodynamic assessment of the Fe-Te system. Part II: thermodynamic modeling, J. Alloys Compd. 767 (2018) 883–893, https://doi.org/10.1016/J.JALLCOM.2018.07.051.

[38] H. Furuya, M. Saito, M. Sugisaki, Corrosion behavior of stainless steel by oxygen and tellurium at low oxygen potentials, J. Nucl. Mater. 154 (1988) 128–137, https://doi.org/10.1016/0022-3115(88)90126-2.

[39] A.R. Miedema, On the heat of formation of solid alloys. II, J. Less-Common Met. 46 (1976) 67–83, https://doi.org/10.1016/0022-5088(76)90180-6.

[40] D. Boa, S. Hassam, J. Rogez, K.P. Kotchi, The iron–antimony system: enthalpies of formation of the FeSb$_2$ and ε-FeSb phases, J. Alloys Compd. 365 (2004) 228–232, https://doi.org/10.1016/S0925-8388(03)00685-6.

[41] B. Eichler, H. Rossbach, H. Gäggeler, Thermochemical characterization of binary tellurium-metal systems, J. Less-Common Met. 163 (1990) 297–310, https://doi.org/10.1016/0022-5088(90)90596-C.